Fast and Accurate Calculation of System-Level ESD Noise Coupling to a Signal Trace by PEEC Model Decomposition

Junsik Park, Jongsung Lee, Byongsu Seol, and Jingook Kim, *Senior Member, IEEE*

***Abstract*— A fast and accurate calculation method of system-level electrostatic discharge (ESD) noise coupling based on model decomposition of the partial element equivalent circuit is proposed. The proposed method can significantly reduce the calculation time without loss of accuracy by separating small victim signal traces from large aggressor structures such as ground planes and ESD gun strap. Using the method, the ESD noise coupling at the terminations of a victim signal trace is rigorously calculated and validated with measurements and full-wave simulations in both frequency and time domains.**

***Index Terms*— Electrostatic discharge (ESD), electromagnetic immunity, model decomposition, noise coupling, partial element equivalent circuit (PEEC), transmission line.**

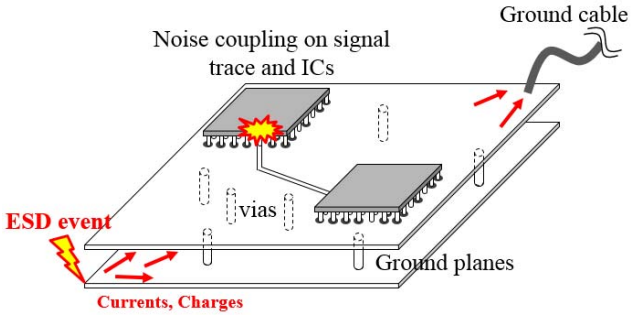

Fig. 1. Illustration of system-level ESD noise coupling.

I. Introduction

THE electromagnetic immunity of electronic systems becomes a more critical issue with the booming development of smart mobile and wearable devices. Any electronic system should be designed to be immune to unexpected external noises, such as surge, burst–electrical fast transients, and electrostatic discharge (ESD) [1]. ESD is one of the most critical noisy events for integrated circuits (ICs), as depicted in Fig. 1. Since ESD events create a high current peak with fast rise time, it can cause unexpected large noise coupled on signal traces and result in malfunctions of the ICs. Hence, for system-level electromagnetic immunity design, it is important to estimate the system-level ESD noise coupling at the various signal traces in the electronic system and figure out whether it can cause functional failures of the ICs or not.

Several electromagnetic numerical methods, such as the finite-difference time domain and finite integration technique, have been utilized to calculate noise coupling due to ESD events [2]–[8]. In these numerical simulations, most of the simulation time is consumed in simulation of the large ground geometries, such as the ground planes of printed circuit boards (PCBs) and ESD gun structures, rather than the small victim signal traces. It is very inefficient to simulate various case studies of the small victim traces with the identical large ground geometries. Recently, the partial element equivalent circuit (PEEC) method has been applied to calculate the ESD coupled noise efficiently.

The inductive and capacitive ESD noise couplings to a conductor loop or conductor pieces were calculated in [9], and the ESD noise coupling to a microstrip line was also quickly calculated in [10]. The transient ESD noise waveforms can be obtained from the solution in frequency domain, since the contact mode ESD is dominated by linear circuit elements. In these works, the victim geometries such as the conductor loop, conductor pieces, and microstrip lines are handled separately from the large aggressor geometries such as the PCB planes and the ESD gun structures by neglecting the reverse coupling effect from the victim to the aggressor for efficient calculation. The conductor loop or conductor pieces in [9] as the simple victim structures are quite small and relatively far from the aggressor structure, and the reverse coupling is actually negligible. However, the microstrip line in [10] as a more realistic victim geometry has significant interaction with the aggressor reference planes, and the results calculated by ignoring the reverse coupling have some inherent errors. Therefore, an improved calculation method by maintaining the interaction between the victim and the aggressor should be developed.

There have also been many researches on the IC switching noise coupling from power-ground planes to signal traces in packages or PCBs [11]–[15]. The physics of system-level ESD noise coupling to signal traces is similar but more complicated than the IC switching noise coupling problem. The system

Manuscript received February 20, 2016; revised July 5, 2016 and September 20, 2016; accepted September 23, 2016. Date of publication October 31, 2016; date of current version January 26, 2017. This work was supported in part by the Basic Science Research Program through the National Research Foundation of Korea (NRF) funded by the Ministry of Education (2013R1A1A2058045).

J. Park and J. Kim are with the School of Electrical and Computer Engineering (ECE), Ulsan National Institute of Science and Technology, Ulsan 689-798, South Korea (e-mail: pjs3300@unist.ac.kr; jingook@unist.ac.kr).

J. Lee and B. Seol are with the Global Technology Center, Samsung Electronics Company, Ltd., Suwon 442-742, South Korea.

Color versions of one or more of the figures in this paper are available online at http://ieeexplore.ieee.org.

Digital Object Identifier 10.1109/TMTT.2016.2615620

ESD noise is generated by an external ESD gun, whereas the IC switching noise is generated by small ICs inside the structure. The ESD gun and straps are also involved in the coupling in addition to the ground planes, and the overall size of the aggressor structure is largely increased. A generalized approach that can decompose small victim traces from large aggressor parts should be very effective in the ESD noise coupling problem.

In this paper, the PEEC model written in the modified nodal analysis (MNA) matrix is rigorously decomposed to the aggressor part and the victim part. The MNA matrix for the victim part is then simplified to a transmission line model (TLM) by maintaining the coupling sources from the aggressor part. The reverse coupling effects from the victim to the aggressor structures are successfully included in this procedure. The coupled voltages at the terminations of signal traces are calculated and validated by comparison with measurements and full-wave simulations both in the frequency and time domains.

A general full-wave simulator solves the large aggressor structure and the small victim at the same time, while the proposed method solves the aggressor geometry only once for multiple victims with the same aggressor structure. As a result, the proposed calculation method of the ESD noise coupling is much faster than full-wave simulations without loss of accuracy, especially when various victim structures on the same aggressor geometry are solved. Moreover, the proposed calculation method can be applied to not only ESD noise coupling but also to other types of noise coupling problems such as the IC switching noise coupling to a signal trace.

A test geometry for ESD noise analysis will be introduced and modeled using PEEC method in Section II. In Section III, the PEEC model for total geometry will be decomposed into aggressor and victim parts, and the victim part will be simplified to a TLM by mathematical and physical procedures. The proposed calculation method will be validated with full-wave simulations and measurements in the frequency domain for various victim cases in Section IV. Finally, the circuit model of ESD generator will be incorporated in the proposed modeling method, and transient ESD noise waveforms will be calculated and compared with the measured results in Section V.

II. Geometry for ESD Noise Coupling Analysis and Total PEEC Model

The total PEEC model of a test geometry for the ESD noise coupling analysis is built in this section. The input and transfer impedances of the model are then validated by comparison with simulation results using the commercial finite element method solver, HFSS.

A. Test Geometry for ESD Noise Coupling Analysis

The test geometry for the ESD noise coupling analysis is illustrated in Fig. 2. Fig. 2(a) shows the structures of the ESD gun strap and PCB metal planes. The two metal planes could be a pair of power-ground planes or both ground planes. Assume that the ESD current is injected to the bottom plane through a via connection. The ESD current returns through the ESD gun strap with a 2-m length, which is connected

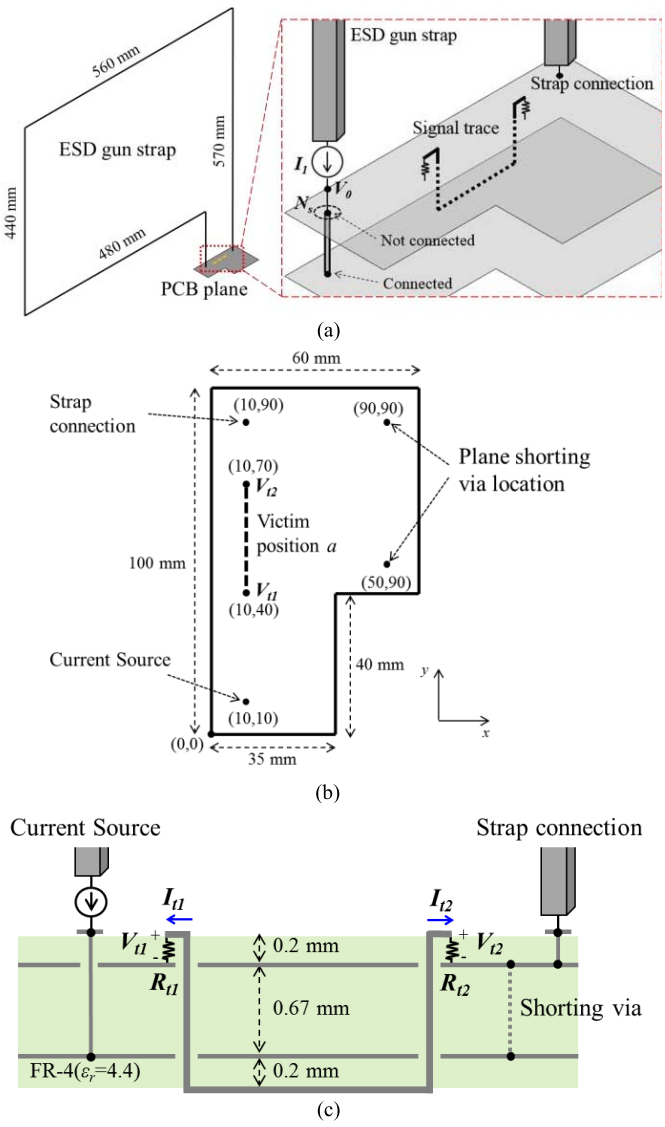

Fig. 2. Test geometry for the ESD noise coupling analysis. (a) Structures of the ESD gun strap and PCB metal planes. (b) Top view of the PCB metal planes with a victim trace at the position a. (c) Side view.

to the PCB top plane at the other end. The top view of the PCB metal planes is shown in Fig. 2(b). Two kinds of PCB structures based on the existence of shorting vias connected between the two planes are considered herein. One is named the "w/o shorting via" case, where the two planes are separated from each other without the shorting vias. The other is named the "w/ shorting via" case, where the two planes are connected through two shorting vias located at the coordinates of (50, 90) and (90, 90) mm, as depicted in Fig. 2(b). The shape of two metal planes is identical in both the cases. The spacing between planes is 0.67 mm and is filled with FR4 dielectric material.

A single microstrip line is chosen as a target victim structure here. The microstrip line is routed 30 mm long at the bottom layer of the PCB, and both ends of the line are connected to the top metal plane through two via transitions and termination resistances R_{t1} and R_{t2}. The side view of victim structure is shown in Fig. 2(c). The dielectric thickness for the

microstrip line is 0.2 mm and the line width is 0.3778 mm. In Sections II and III, the victim position a in the "w/ shorting" case is chosen for validation of the calculation method. In Sections IV and V, two additional victim positions will also be calculated to investigate the noise coupling dependency on the victim positions.

B. Calculation and Validation of the Total PEEC Model

The current and charge densities in the total geometry are discretized into volume and surface mesh cells for the PEEC modeling. The circuit interpretation of the electric field integral equation (EFIE) in the metal geometry is then obtained using the PEEC method. The EFIE can be written as [16]–[20]

$$\vec{E}_i(\vec{r},\omega) = \frac{\vec{J}(\vec{r},\omega)}{\sigma} + j\omega\frac{\mu}{4\pi}\int_{v'}\frac{\vec{J}(\vec{r}',\omega)e^{-jk|\vec{r}-\vec{r}'|}}{|\vec{r}'-\vec{r}|}dv' + \frac{\nabla}{4\pi\varepsilon_0}\int_{s'}\frac{\rho(\vec{r}',\omega)e^{-jk|\vec{r}-\vec{r}'|}}{|\vec{r}'-\vec{r}|}ds' \quad (1)$$

where $\vec{E}_i$ is an applied electric field, J is the current density in the conductor with conductivity σ, k is the propagation constant, and ρ is the surface charge density, respectively. The first and second terms on the right-hand side represent the electric fields due to resistance and inductance, while the third term represents the electric field due to capacitance. The time retardation from the source position $\vec{r}'$ to the observation position $\vec{r}$ is represented as the exponential parts in the second and third terms.

The continuity equation for charge conservation at every mesh node of conductor and dielectric medium can be expressed as

$$\nabla\cdot\vec{J}(\vec{r},\omega) + j\omega\rho(\vec{r},\omega) = 0. \quad (2)$$

The EFIE and the continuity equation provide numerous KVL and KCL equations, respectively, which can be solved using the MNA matrix. The MNA matrix for the geometry of Fig. 2 is expressed in (3), as shown at the bottom of this page, whereby the submatrices and subvectors are summarized in Table I. From now on, for convenience, the total geometry will be divided into aggressor parts and the victim part. The aggressor part represents all the geometry except the signal trace, whereas the victim part represents only the signal trace. The subscript notations a and v represent the aggressor and the victim structures, respectively. For example, the vectors, $\bar{Q}_a$, $\bar{Q}_v$, $\bar{I}_a$, $\bar{I}_v$ represent the unknown charges and currents on the aggressor mesh cells and the victim mesh cells, respectively. Also, the $\overline{\overline{P_{v-a,r}}}$ means the potential coefficient matrix including the retardation effect from the aggressor mesh cells to the victim ones.

The first line in (3) represents the source condition, where the current source I_1 of value 1 is injected. The second and third lines represent the KCL of the aggressor and victim geometries, respectively. The next three lines represent the KVL of the aggressor and victim geometries. The bottom two

TABLE I
SUBMATRICES AND SUBVECTORS IN THE MNA MATRIX

Matrix	Information
V_0	Input voltage at the source node
I_1	Injected current at the source node
$\overline{\overline{E}}$	Identity matrix.
$\overline{N_s}$	1 at source position, otherwise zero. Dimension : (1 × 5589)
$\overline{\overline{N_m}}$	Connectivity matrix. (14701 × 5619)
$\overline{\overline{P_r}}$	Matrix of the partial potential coefficients with retardation effect, $Pp_{ij,r}$. (5619 × 5619)
$\overline{\overline{L_r}}$	Matrix of the partial inductance with retardation effect, $Lp_{ij,r}$. (14701 × 14701)
$\overline{\overline{R}}$	Matrix of the partial resistance. (14701 × 14701)
$\overline{\overline{Z_r}}$	Matrix of the partial impedances as $\overline{\overline{Z_r}} = j\omega\overline{\overline{L_r}} + \overline{\overline{R}}$. (14701 × 14701)
$\overline{N_{t1,a}}, \overline{N_{t2,a}}$	1 at termination points on aggressor, otherwise zero. (1 × 5589)
$\overline{N_{t1,v}}, \overline{N_{t2,v}}$	1 at termination points on victim, otherwise zero. (1 × 30)
R_{t1}, R_{t2}	Termination resistances of the victim trace.
$\overline{Q_a}, \overline{Q_v}$	Charges on the aggressor and victim mesh cells. (1 × 5589) / (1 × 30)
$\overline{I_a}, \overline{I_v}$	Currents on the aggressor and victim mesh cells. (1 × 14672) / (1 × 29)
I_{t1}, I_{t2}	Currents at the victim terminations. (1 × 1)
$\overline{N_{sg}}$	1 at the end of strap, otherwise zero. (1 × 5589)

$$\overbrace{\begin{bmatrix} 0 & \overline{0} & \overline{0} & 1 & \overline{0} & \overline{0} & 0 & 0 \\ \overline{0}^T & s\overline{\overline{E}} & \overline{\overline{0}} & -\overline{N_s}^T & -\overline{\overline{N_{m,a}}}^T & \overline{\overline{0}} & -\overline{N_{t1,a}}^T & -\overline{N_{t2,a}}^T \\ \overline{0}^T & \overline{\overline{0}} & s\overline{\overline{E}} & \overline{0}^T & \overline{\overline{0}} & -\overline{\overline{N_{m,v}}}^T & \overline{N_{t1,v}}^T & \overline{N_{t2,v}}^T \\ -1 & \overline{N_s}\,\overline{\overline{P_{a-a,r}}} & \overline{N_s}\,\overline{\overline{P_{a-v,r}}} & 0 & \overline{0} & \overline{0} & 0 & 0 \\ \overline{0}^T & \overline{\overline{N_{m,a}}}\,\overline{\overline{P_{a-a,r}}} & \overline{\overline{N_{m,a}}}\,\overline{\overline{P_{a-v,r}}} & \overline{0}^T & \overline{\overline{Z_{a-a,r}}} & \overline{\overline{Z_{a-v,r}}} & \overline{0}^T & \overline{0}^T \\ \overline{0}^T & \overline{\overline{N_{m,v}}}\,\overline{\overline{P_{v-a,r}}} & \overline{\overline{N_{m,v}}}\,\overline{\overline{P_{v-v,r}}} & \overline{0}^T & \overline{\overline{Z_{v-a,r}}} & \overline{\overline{Z_{v-v,r}}} & \overline{0}^T & \overline{0}^T \\ 0 & \overline{N_{t1,v}}\,\overline{\overline{P_{v-a,r}}} - \overline{N_{t1,a}}\,\overline{\overline{P_{a-a,r}}} & \overline{N_{t1,v}}\,\overline{\overline{P_{v-v,r}}} - \overline{N_{t1,a}}\,\overline{\overline{P_{a-v,r}}} & 0 & \overline{0} & \overline{0} & -R_{t1} & 0 \\ 0 & \overline{N_{t2,v}}\,\overline{\overline{P_{v-a,r}}} - \overline{N_{t2,a}}\,\overline{\overline{P_{a-a,r}}} & \overline{N_{t2,v}}\,\overline{\overline{P_{v-v,r}}} - \overline{N_{t2,a}}\,\overline{\overline{P_{a-v,r}}} & 0 & \overline{0} & \overline{0} & 0 & -R_{t2} \end{bmatrix}}^{\overline{\overline{A}}} \overbrace{\begin{bmatrix} V_0 \\ \overline{Q_a}^T \\ \overline{Q_v}^T \\ I_1 \\ \overline{I_a}^T \\ \overline{I_v}^T \\ I_{t1} \\ I_{t2} \end{bmatrix}}^{\text{Unknown } (\overline{C})} = \overbrace{\begin{bmatrix} 1 \\ -\overline{N_{sg}}^T \\ \overline{0}^T \\ 0 \\ \overline{0}^T \\ \overline{0}^T \\ 0 \\ 0 \end{bmatrix}}^{\text{Source } (\overline{B})} \quad (3)$$

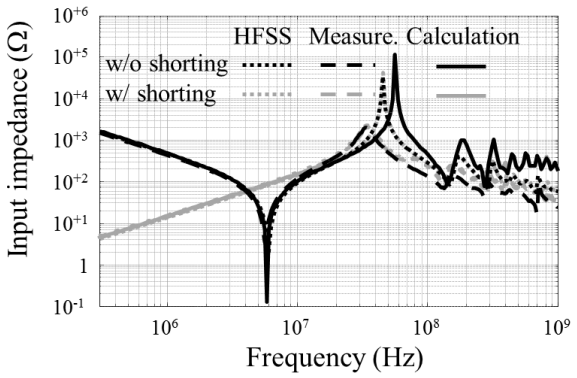

Fig. 3. Input impedance seen at the current injection point obtained from the PEEC calculation, HFSS, and the measurement.

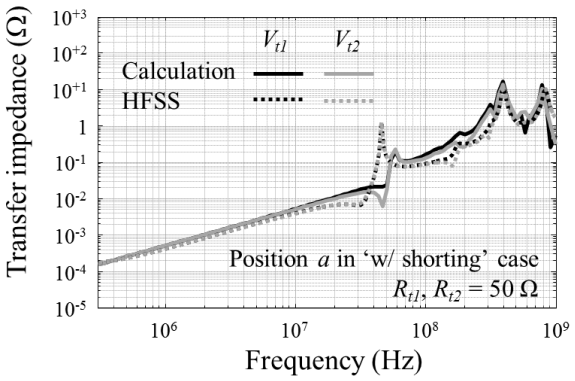

Fig. 4. Transfer impedances at the terminations of the victim signal trace in the position a of the "w/ shorting" case.

lines represent the KVL at the terminations connected between the aggressor and victim structures.

The generalized equation for the partial inductance with retardation effect is represented as [16]

$$Lp_{ij,r} = \frac{\mu}{4\pi}\frac{1}{a_j a_i}\int_{a_i}\int_{l_i}\int_{a_j}\int_{l_j}\frac{e^{-j\beta|\vec{r}_i-\vec{r}_j|}}{|\vec{r}_i-\vec{r}_j|}d\vec{l}_j\cdot d\vec{l}_i da_j da_i \tag{4}$$

where β is the propagation constant, $\vec{l}$ and a are the length and the cross-sectional area of a current mesh cell, respectively, and $e^{-j\beta|\vec{r}_i-\vec{r}_j|}$ represents the retardation effect between ith and jth mesh cells.

Also, the generalized equation for the potential coefficient with the retardation effect is given as [16]

$$Pp_{ij,r} = \frac{1}{4\pi\varepsilon}\frac{1}{s_i s_j}\int_{S_i}\int_{S_j}\frac{e^{-j\beta|\vec{r}_i-\vec{r}_j|}}{|\vec{r}_i-\vec{r}_j|}ds_j ds_i \tag{5}$$

where s is the surface area of a charge mesh cell.

The partial inductance $Lp_{ij,r}$ and the partial potential coefficient $Pp_{ij,r}$ for various mesh cells can be calculated from approximated closed-form expressions [17]–[21]. In this paper, the metal planes were discretized into rectangular mesh cells of 2 mm × 2 mm. The strap has been discretized into cuboid cells with four rectangular sides of height 10 mm, and the mutual inductance and partial potential coefficients between strap cells and between strap-to-plane cells have been calculated using the equations for the plane-to-plane cells in [17] and [18]. The dielectric material is also divided into cuboid cells and modeled as the series connections of partial resistances, inductances, excess capacitances, and voltage drops across the excess capacitance [20]. The dimensions of all the vectors and matrices for a case of the PEEC calculations are also indicated in Table I.

The input impedance at the current source point is calculated with the PEEC MNA equation (3), and is compared with HFSS and the measurement results in Fig. 3. The capacitive behavior is shown at the impedance below 5 MHz in the "w/o shoring" case due to the plane capacitance inside the PCB, while the inductive behavior is shown in in the "w/ shoring" case due to the conductive path through the shorting vias.

The overall impedance trends and the values below 30 MHz agree very well between PEEC and HFSS, but there is some discrepancy at the frequency of the first impedance peak. The discrepancy is attributed to the inaccurate partial capacitance modeling of the strap geometry. To reduce the PEEC modeling complexity of the long ESD gun strap, the strap was discretized into the cuboid mesh cells at a height of 10 mm, and the potential coefficients of the four rectangular sides are averaged and merged into a single strap node per cuboid, which may cause the inaccurate distributed capacitance values of the strap. The measurement setup and conditions will be explained in Section IV. Compared with the measurement, the PEEC calculation and HFSS simulation show sharp peaks at the resonance frequency below 100 MHz, probably because the resistive loss at the large strap geometry is not accurately modeled.

The voltages at the terminations of the victim microstrip line induced by the current source are also calculated by (3) and compared with HFSS. V_{t1} and V_{t2} represent the two termination voltages in the time and frequency domains. The transfer impedance in the frequency domain is the same as the termination voltages since the injected current I_1 is set as 1 A. The termination resistances R_{t1} and R_{t2} are both 50 Ω. Fig. 4 shows the transfer impedances in the "w/ shorting" case. The results validate the good accuracy of the PEEC MNA solutions of (3).

III. Proposed Calculation Method Based on Model Decomposition

A. Model Decomposition Into Aggressor and Victim Parts

In the ESD noise coupling analysis, the victim signal trace is usually much smaller than the noise aggressing structure such as the PCB ground planes and ESD gun strap. Electromagnetic computations of small geometries together with large ones requires a large number of meshes, increasing the computation time inefficiently. Also, the ESD noise aggressor part is usually fixed and various victim cases of different lengths, positions, and paths need to be simulated. Hence, if the victim geometry can be separately handled from the aggressor geometry, the system-level ESD noise can be analyzed very efficiently.

The separation process is possible since the charges and currents are obtained as the solution of the PEEC calculation. Any full-wave numerical methods based on the integral equations, such as the method of moments, would be able to handle the victim and aggressor geometries separately. However, for further simplification of the victim model into a transmission

line, as explained in the following sections, the PEEC model is the most effective as the PEEC is implemented in the circuit fashion. The solution vector of the aggressor geometry can be directly used as the inductive and capacitive coupling sources for the particular simple victims [9]. A rigorous approach that can solve the noise coupling to a general signal trace is developed herein.

The physical concept of the proposed calculation method is introduced at first. Assume two structures according to the existence of a victim trace, as shown in Fig. 5. Fig. 5(a) shows the case with only aggressor structure without the victim geometry. The charges and currents, which are named Q_{a1} and I_{a1}, will be induced on the aggressor geometry by the current source. Next, assume the victim geometry is added to the aggressor geometry as shown in Fig. 5(b). The charge and current distribution on the aggressor are changed from (Q_{a1} and I_{a1}) to ($Q_{a1}+Q_{a2}$ and $I_{a1}+I_{a2}$) due to the victim geometry. The variations in the charges and currents on the aggressor geometry caused by the victim structure are named Q_{a2} and I_{a2}. At the same time, the charges and currents on the victim Q_v and I_v are induced due to the charges and currents of the aggressor.

The procedure in Fig. 5 can be rigorously derived by decomposing the PEEC MNA equation (3). To begin with, the MNA equation $\overline{\overline{A}}\,\overline{C}=\overline{B}$ of (3) is written again as

$$\overline{\overline{A}}\left(\overbrace{\begin{bmatrix} V_1 \\ \overline{Q_{a1}}^T \\ \overline{0}^T \\ I_1 \\ \overline{I_{a1}}^T \\ \overline{0}^T \\ 0 \\ 0 \end{bmatrix}}^{\overline{C_a}} + \overbrace{\begin{bmatrix} V_2 \\ \overline{Q_{a2}}^T \\ \overline{Q_v}^T \\ 0 \\ \overline{I_{a2}}^T \\ \overline{I_v}^T \\ I_{t1} \\ I_{t2} \end{bmatrix}}^{\overline{C_v}}\right) = \left(\overbrace{\begin{bmatrix} 1 \\ -\overline{N_{sg}}^T \\ \overline{0}^T \\ 0 \\ \overline{0}^T \\ \overline{V_{v-a}}^T \\ V_{t1-a} \\ V_{t2-a} \end{bmatrix}}^{\overline{B_a}} + \overbrace{\begin{bmatrix} 0 \\ \overline{0}^T \\ \overline{0}^T \\ 0 \\ \overline{0}^T \\ -\overline{V_{v-a}}^T \\ -V_{t1-a} \\ -V_{t2-a} \end{bmatrix}}^{\overline{B_v}}\right) \tag{6}$$

where

$$\begin{aligned} V_0 &= V_1 + V_2 \\ \overline{Q_a} &= \overline{Q_{a1}} + \overline{Q_{a2}} \\ \overline{I_a} &= \overline{I_{a1}} + \overline{I_{a2}} \\ \overline{V_{v-a}}^T &= \overline{\overline{N_{m,v}}}\;\overline{\overline{P_{v-a,r}}}\;\overline{Q_{a1}}^T + \overline{\overline{Z_{v-a,r}}}\;\overline{I_{a1}}^T \\ V_{t1-a} &= \overline{N_{t1,v}}\;\overline{\overline{P_{v-a,r}}}\;\overline{Q_{a1}}^T - \overline{N_{t1,a}}\;\overline{\overline{P_{a-a,r}}}\;\overline{Q_{a1}}^T \\ V_{t2-a} &= \overline{N_{t2,v}}\;\overline{\overline{P_{v-a,r}}}\;\overline{Q_{a1}}^T - \overline{N_{t2,a}}\;\overline{\overline{P_{a-a,r}}}\;\overline{Q_{a1}}^T. \end{aligned}$$

The unknown vector $\overline{C}$ is divided into $\overline{C_a}$ and $\overline{C_v}$, and the source vector $\overline{B}$ is divided into $\overline{B_a}$ and $\overline{B_v}$, resulting in two separated equations as

$$\overline{\overline{A}}\,\overline{C_a} = \overline{B_a} \tag{7}$$

$$\overline{\overline{A}}\,\overline{C_v} = \overline{B_v}. \tag{8}$$

In (7), the vector $\overline{B_a}$ contains the source condition injected at the aggressor in addition to several terms related to the victim structure $\overline{V_{v-a}}$, V_{t1-a}, V_{t2-a}, which are necessary to make all the equations including the victim-related terms be indeterminate. By removing the indeterminate equations, the MNA equation (7) is simplified as

$$\begin{bmatrix} 0 & \bar{0} & 1 & \bar{0} \\ \bar{0}^T & s\overline{\overline{E}} & -\overline{N_s}^T & -\overline{\overline{N_{m,a}}}^T \\ -1 & \overline{N_s}\;\overline{\overline{P_{a-a,r}}} & 0 & \bar{0} \\ \bar{0}^T & \overline{\overline{N_{m,a}}}\;\overline{\overline{P_{a-a,r}}} & \overline{0}^T & \overline{\overline{Z_{a-a,r}}} \end{bmatrix} \begin{bmatrix} V_1 \\ \overline{Q_{a1}}^T \\ I_1 \\ \overline{I_{a1}}^T \end{bmatrix} = \begin{bmatrix} 1 \\ -\overline{N_{sg}}^T \\ 0 \\ \overline{0}^T \end{bmatrix}. \tag{9}$$

All the elements in (9) consist of only the aggressor geometry without the victim geometry, as shown in Fig. 5(a). The charge and current distributions on the aggressor structure Q_{a1} and I_{a1} induced by the current source injection can then be solved by (9), which will be called the "aggressor MNA equation."

Next, in (8), which will be called the "victim MNA equation," Q_{a1} and I_{a1} appear as source terms in the $\overline{B_v}$ vector accordingly. Specifically, $\overline{V_{v-a}}$ indicates the capacitive and inductive coupling from the aggressor to the victim cells. $\overline{V_{t1-a}}$ and $\overline{V_{t2-a}}$ indicate the voltages induced along the victim terminations due to the connections between the victim and aggressor cells.

As results, Q_v and I_v in the $\overline{C_v}$ vector represent the charges and currents on the victim structure induced by Q_a and I_a. Also, the Q_{a2} and I_{a2} represent the variation of the aggressor charges and currents due to existence of the victim structure, which implies the reverse coupling effects from the victim to the aggressor structure. Finally, the total MNA equation of (3) has been successfully decomposed to

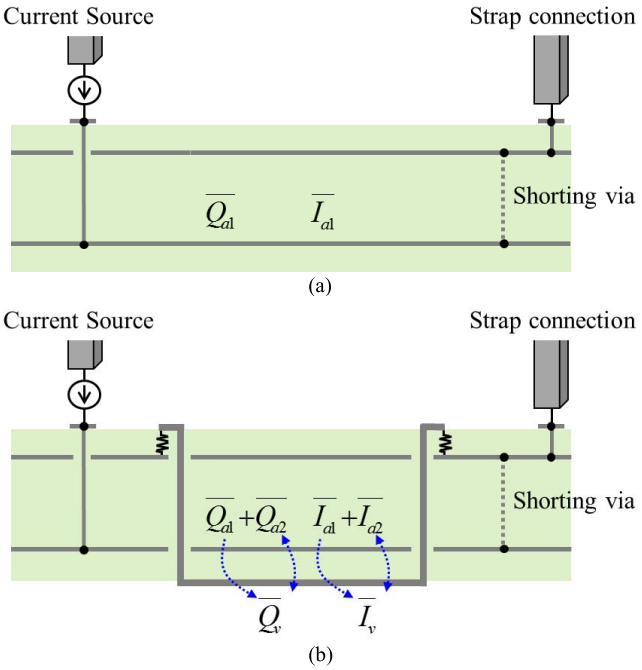

Fig. 5. Charges and currents induced by the current source condition (a) in the aggressor structure only and (b) in the total structure with both aggressor and victim geometries.

the two step problems of Fig. 5(a) and (b). Nevertheless, the huge aggressor geometry is still contained in the victim MNA equation of (8), resulting in no computational benefits.

If the reverse coupling terms from the victim to the aggressor $\overline{\overline{P_{a-v,r}}}\,\overline{Q_v}$ and $\overline{\overline{L_{a-v,r}}}\,\overline{I_v}$ are neglected, the victim MNA equation is greatly simplified as

$$\begin{bmatrix} s\overline{\overline{E}} & -\overline{\overline{N_{m,v}}}^T & \overline{N_{t1}}^T & \overline{N_{t2}}^T \\ \overline{\overline{N_{m,v}}} & \overline{\overline{P_{v-v,r}}} & \overline{\overline{Z_{v-v,r}}} & \bar{0}^T & \bar{0}^T \\ \overline{N_{t1}} & \overline{\overline{P_{v-v,r}}} & \bar{0} & -R_{t1} & 0 \\ \overline{N_{t2}} & \overline{\overline{P_{v-v,r}}} & \bar{0} & 0 & -R_{t2} \end{bmatrix} \begin{bmatrix} \overline{Q_v}^T \\ \overline{I_v}^T \\ I_{t1} \\ I_{t2} \end{bmatrix} = \begin{bmatrix} 0 \\ -\overline{V_{v-a}}^T \\ -V_{t1-a} \\ -V_{t2-a} \end{bmatrix} \tag{10}$$

which is the same as [10, eq. (7)].

However, there is a limitation in the accuracy of (10), since the interaction between the victim and the aggressor could be significant. Therefore, the way to effectively reflect the aggressor geometry in the calculation of the victim MNA equation should be found. Since the victim structure of interest here is basically a transmission line, the TLM with the per-unit-length (PUL) inductance and capacitance can be a good approximation of the victim PEEC circuit model. A TLM is described in terms of the voltages and currents instead of the charges and currents. Accordingly, the victim MNA equations (8) in terms of the charges and currents should be converted into those of voltages and currents. The MNA equations expressed with the voltages and currents are then replaced with the TLM with PUL elements in the following sections.

B. Victim Model With Frequency-Independent Circuit Parameters

The PEEC MNA model is the full-wave numerical solution. For a large geometry, the retardation effect between the distant cells should be considered, which are included in the partial inductance and potential coefficient matrices in the retarded PEEC model. Therefore, the MNA equations for the large aggressor structure are directly expressed in terms of the charges and potential coefficient matrix, as shown in the two MNA equations (7) and (8). The retardation effect between Q_{a2} and Q_v in the victim MNA equation, however, can be negligible, since the charge of the small victim transmission line, Q_v, interacts predominantly with only the charge of the aggressor cells near the victim geometry, Q_{a2}, which play the role of reference plane for signal propagation. By removing the retardation terms in the coupling between Q_{a2} and Q_v, the potential coefficient matrix for the victim part is frequency-independent, which is then inversed to the frequency-independent capacitance matrix. Thus, the victim trace can be modeled with frequency-independent R-L-G-C parameters, but there is no significant loss of accuracy since the retardations in the coupling from Q_{a1} are still retained.

The mathematical procedure starts from the relation between the voltages and charges as

$$\begin{bmatrix} \overline{\overline{P_{a-a,r}}} & \overline{\overline{P_{a-v,r}}} \\ \overline{\overline{P_{v-a,r}}} & \overline{\overline{P_{v-v,r}}} \end{bmatrix} \begin{bmatrix} \overline{Q_a}^T \\ \overline{Q_v}^T \end{bmatrix} = \begin{bmatrix} \overline{V_a}^T \\ \overline{V_v}^T \end{bmatrix}. \tag{11}$$

The charge and voltage vectors are similarly decomposed into two parts as

$$\begin{bmatrix} \overline{\overline{P_{a-a,r}}} & \overline{\overline{P_{a-v,r}}} \\ \overline{\overline{P_{v-a,r}}} & \overline{\overline{P_{v-v,r}}} \end{bmatrix} \left(\begin{bmatrix} \overline{Q_{a1}}^T \\ \overline{0}^T \end{bmatrix} + \begin{bmatrix} \overline{Q_{a2}}^T \\ \overline{Q_v}^T \end{bmatrix} \right) = \begin{bmatrix} \overline{\overline{P_{a-a,r}}}\,\overline{Q_{a1}}^T \\ \overline{\overline{P_{v-a,r}}}\,\overline{Q_{a1}}^T \end{bmatrix} + \begin{bmatrix} \overline{V_a}^T - \overline{\overline{P_{a-a,r}}}\,\overline{Q_{a1}}^T \\ \overline{V_v}^T - \overline{\overline{P_{v-a,r}}}\,\overline{Q_{a1}}^T \end{bmatrix}.$$

After cancelling the first vector terms on the left and right sides, the relation between the voltages and charges for the "victim MNA equation" are obtained. As aforementioned, the retardation effect for Q_{a2} and Q_v is neglected, resulting in

$$\begin{bmatrix} \overline{\overline{P_{a-a}}} & \overline{\overline{P_{a-v}}} \\ \overline{\overline{P_{v-a}}} & \overline{\overline{P_{v-v}}} \end{bmatrix} \begin{bmatrix} \overline{Q_{a2}}^T \\ \overline{Q_v}^T \end{bmatrix} = \begin{bmatrix} \overline{V_a}^T - \overline{\overline{P_{a-a,r}}}\,\overline{Q_{a1}}^T \\ \overline{V_v}^T - \overline{\overline{P_{v-a,r}}}\,\overline{Q_{a1}}^T \end{bmatrix} \tag{12}$$

where the $\overline{\overline{P_{a-a}}}$, $\overline{\overline{P_{a-v}}}$, $\overline{\overline{P_{v-a}}}$, and $\overline{\overline{P_{v-v}}}$ represent the matrices of the static potential coefficients without the retardation effect.

The charges for the victim MNA equations are finally written in terms of the voltages as

$$\begin{bmatrix} \overline{Q_{a2}}^T \\ \overline{Q_v}^T \end{bmatrix} = \begin{bmatrix} \overline{\overline{C_{a-a}}} & \overline{\overline{C_{a-v}}} \\ \overline{\overline{C_{v-a}}} & \overline{\overline{C_{v-v}}} \end{bmatrix} \begin{bmatrix} \overline{V_a}^T - \overline{\overline{P_{a-a,r}}}\,\overline{Q_{a1}}^T \\ \overline{V_v}^T - \overline{\overline{P_{v-a,r}}}\,\overline{Q_{a1}}^T \end{bmatrix} \tag{13}$$

where

$$\begin{bmatrix} \overline{\overline{C_{a-a}}} & \overline{\overline{C_{a-v}}} \\ \overline{\overline{C_{v-a}}} & \overline{\overline{C_{v-v}}} \end{bmatrix} = \begin{bmatrix} \overline{\overline{P_{a-a}}} & \overline{\overline{P_{a-v}}} \\ \overline{\overline{P_{v-a}}} & \overline{\overline{P_{v-v}}} \end{bmatrix}^{-1}.$$

By substituting (13) into (8), removing the retardation term related with I_{a2} and I_v, and eliminating the unnecessary first and fourth lines, the victim MNA equations are expressed with the unknown voltages and currents using the capacitance matrix instead of the potential coefficient matrix as

$$\begin{bmatrix} s\overline{\overline{C_{a-a}}} & s\overline{\overline{C_{a-v}}} & -\overline{\overline{N_{m,a}}}^T & \overline{\overline{0}} & -\overline{N_{t1,a}}^T & -\overline{N_{t2,a}}^T \\ s\overline{\overline{C_{v-a}}} & s\overline{\overline{C_{v-v}}} & \overline{\overline{0}} & -\overline{\overline{N_{m,v}}}^T & \overline{N_{t1,v}}^T & \overline{N_{t2,v}}^T \\ \overline{\overline{N_{m,a}}} & \overline{\overline{0}} & \overline{\overline{Z_{a-a}}} & \overline{\overline{Z_{a-v}}} & \overline{0}^T & \overline{0}^T \\ \overline{\overline{0}} & \overline{\overline{N_{m,v}}} & \overline{\overline{Z_{v-a}}} & \overline{\overline{Z_{v-v}}} & \overline{0}^T & \overline{0}^T \\ -\overline{N_{t1,a}} & \overline{N_{t1,v}} & \overline{0} & \overline{0} & -R_{t1} & 0 \\ -\overline{N_{t2,a}} & \overline{N_{t2,v}} & \overline{0} & \overline{0} & 0 & -R_{t2} \end{bmatrix} \times \begin{bmatrix} \overline{V_a}^T - \overline{\overline{P_{a-a,r}}}\,\overline{Q_{a1}}^T \\ \overline{V_v}^T - \overline{\overline{P_{v-a,r}}}\,\overline{Q_{a1}}^T \\ \overline{I_{a2}}^T \\ \overline{I_v}^T \\ I_{t1} \\ I_{t2} \end{bmatrix} = \begin{bmatrix} \overline{0}^T \\ \overline{0}^T \\ \overline{0}^T \\ -\overline{V_{v-a}}^T \\ -V_{t1-a} \\ -V_{t2-a} \end{bmatrix}. \tag{14}$$

The solutions of (14) are compared with those of (8). Fig. 6 shows the coupled voltages at the victim terminations in the position a of the "w/ shorting" case. It is validated that the

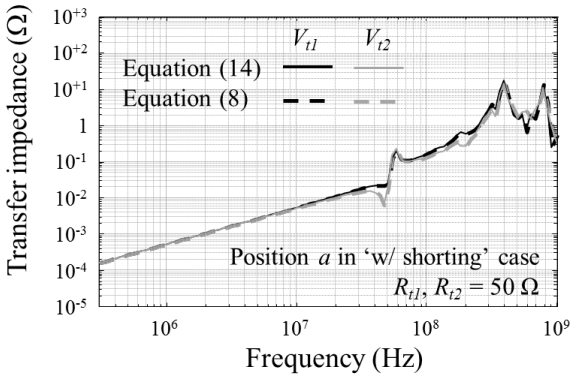

Fig. 6. Comparison between the victim MNA solutions of (8) and (14).

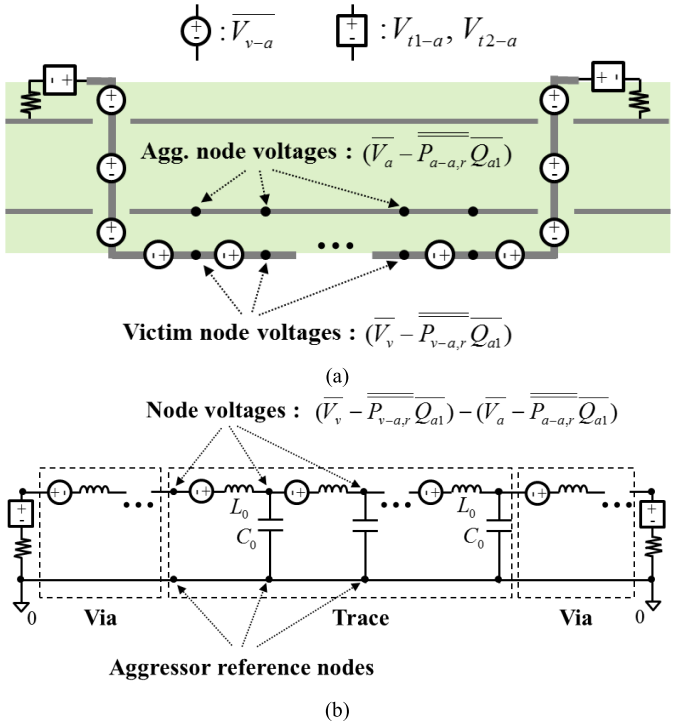

Fig. 7. Model of the victim transmission line. (a) PEEC model for (14). (b) TLM with PUL parameters.

victim MNA matrix has been successfully expressed with the frequency-independent R-L-G-C parameters. The simulations were performed in the frequency domain with 201 points from 300 kHz to 1 GHz. A computer with 64-GB RAM and dual 2.4-GHz quad-core CPU was used in all the calculations. The simulation time of (8) and (14) is 48 h 14 min 49 s and 57 h 41 min 28 s, respectively. The simulation time of (8) is faster than that of (14), as the matrix (8) uses only one unknown charge to construct KCL at a node while the matrix (14) needs all of the unknown voltages for KCL.

C. Simplification of the Victim Model Into the Transmission Line Model

The coupling effects from the aggressor to the victim structure are entirely included as the coupling source terms in (14), which can be modeled as in Fig. 7(a). The circle and square shapes inserted at each victim mesh cell represent the

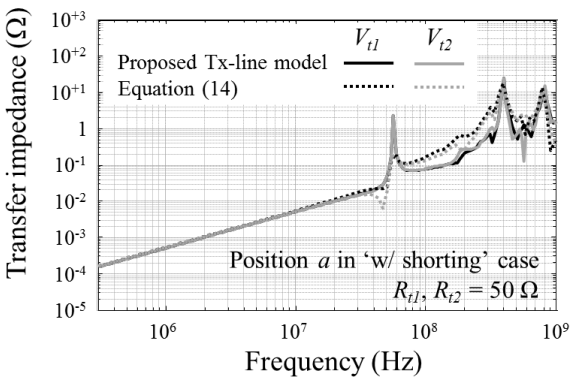

Fig. 8. Comparison between the victim PUL TLM and the victim MNA equation of (14).

coupling sources from the aggressor to the victim trace and terminations, $\overline{V_{v-a}}$, V_{t1-a}, V_{t2-a}, respectively. The capacitive and inductive coupling source $\overline{V_{v-a}}$ is inserted at every mesh cell in the signal trace and via. The conduction coupling source at the terminations $\overline{V_{t1-a}}$ and $\overline{V_{t2-a}}$ are inserted at the connections between the signal trace and the aggressor reference plane. The calculated voltages at the aggressor and victim mesh nodes in the model represent $(\overline{V_a} - \overline{\overline{P_{a-a,r}}\,\overline{Q_{a1}}})$ and $(\overline{V_v} - \overline{\overline{P_{v-a,r}}\,\overline{Q_{a1}}})$, respectively. The final voltage observed between the trace and the reference plane, $(\overline{V_v} - \overline{V_a})$, can then be calculated accordingly.

The resultant electromagnetic field induced in the victim transmission line is predominantly the transverse electromagnetic mode. Therefore, the victim PEEC circuit model in Fig. 7(a) can be simplified using the PUL R-L-G-C TLM and the proper circuit model for the via layer transitions, as shown in Fig. 7(b) [22]–[25]. The loss of the transmission line and the parasitic capacitance at the via pads and barrels are also neglected here for simplicity, as their effects at high frequencies are not significant for the ESD noise coupling analysis. The characteristic impedance, PUL inductance, and capacitance of a lossless microstrip line can be calculated as [23]

$$Z_0 = \frac{87}{\sqrt{\varepsilon_r + 1.41}} \ln\left(\frac{5.98H}{0.8W + T}\right) \ [\Omega] \tag{15}$$

$$C_0 = \frac{26.38(\varepsilon_r + 1.41)}{\ln\left(\frac{5.98H}{0.8W+T}\right)} \ [\text{pF/m}] \tag{16}$$

$$L_0 = Z_0^2 C_0 \tag{17}$$

where ε_r is the dielectric constant, H, W, and T are the height, width, and thickness of the microstrip line, respectively.

The victim TLM consists of the PUL series inductances L_0 in addition to the coupling sources and the PUL shunt capacitances C_0 that are connected to the reference plane. The full-wave victim trace model with partial R-L-G-C parameters in (14) should be equivalent to the TLM with PUL R-L-G-C parameters. The macromodel inductance developed from the full-wave PEEC model is proven equivalent to the L_0 in the TLM [26]. In the TLM, the aggressor reference nodes are set to zero potential, so that the voltages at the transmission line nodes indicate the voltage differences between the vic-

TABLE II
COMPARISON OF THE COMPUTATIONAL TIME

	Proposed Method		HFSS
	Aggressor	Victim	
w/o shorting	50 h 56 m	-	-
Position *a*	-	1 m 29 s	84 h 26 m 25 s
Position *b*	-	1 m 31 s	50 h 24 m 35 s
Position *c*	-	1 m 28 s	89 h 17 m 6 s
Total	51 h 28 s		224 h 8 m 6 s
w/ shorting	50 h 52 m 40 s	-	-
Position *a*	-	1 m 31 s	60 h 41 m 49 s
Position *b*	-	1 m 27 s	69 h 49 m 14 s
Position *c*	-	1 m 25 s	59 h 13 m 58 s
Total	50 h 57 m 2 s		189 h 45 m 1 s

tim nodes and the aggressor nodes as $(\overline{V_v} - \overline{\overline{P_{v-a,r}}\,\overline{Q_{a1}}}) - (\overline{V_a} - \overline{\overline{P_{a-a,r}}\,\overline{Q_{a1}}})$. The final voltages observed between the trace and reference plane of the original total structure are then obtained from $(\overline{V_v} - \overline{V_a})$.

As a result, the final form of the proposed victim trace model is the 1-D TLM instead of the full-wave PEEC model, although the ESD noise coupling from all the aggressor cells calculated using the full-wave PEEC are entirely included as the coupling source terms. The proposed TLM in Fig. 7(b) is validated with the result from the direct solution of (14), as shown in Fig. 8.

IV. CALCULATION AND VALIDATION OF THE NOISE COUPLING TRANSFER IMPEDANCE IN FREQUENCY DOMAIN

The proposed calculation method is applied to various cases, and validated with HFSS simulations and measurements in the frequency domain at first. The induced voltage at one of the terminations V_{t1} is calculated using the TLM of Fig. 7(b) and validated with measurements and HFSS results. The transfer impedance from the excited current to the coupled voltage is measured using the vector network analyzer. Fig. 9 shows the measurement setup, the PCB designs with three victim positions, and the HFSS simulation setup. As shown in Fig. 9(a), the ends of the signal trace are terminated with a 51 Ω SMT resistor at the top plane. The transfer impedances $V_{t1,t2}/I_1$ are measured by connecting the semi-rigid cable directly across the termination resistor. 10 ferrite common-mode (CM) chokes are mounted on the cable to reduce the direct CM noise coupling from the fields. In Sections IV and V, three victim positions depicted in Fig. 9(b) are calculated and validated for the two aggressor cases: "w/o shorting" and "w/ shorting."

Figs. 10 and 11 show the coupled noises in the three victim positions for the "w/o shorting" and "w/ shorting" cases, respectively. One of the termination voltages V_{t1} is shown, and the other termination voltage V_{t2} is also very similar as V_{t1}. As shown in Fig. 10, the transfer impedances have constant values below 30 MHz in the "w/o shorting" case. The overall shapes and the high frequency resonances agree very well between the measurement, the HFSS, and the calculation. As aforementioned, the discrepancy at the first resonance peak is attributed to the inaccurate partial capacitance modeling of the aggressor strap geometry. In the case of "w/ shorting,"

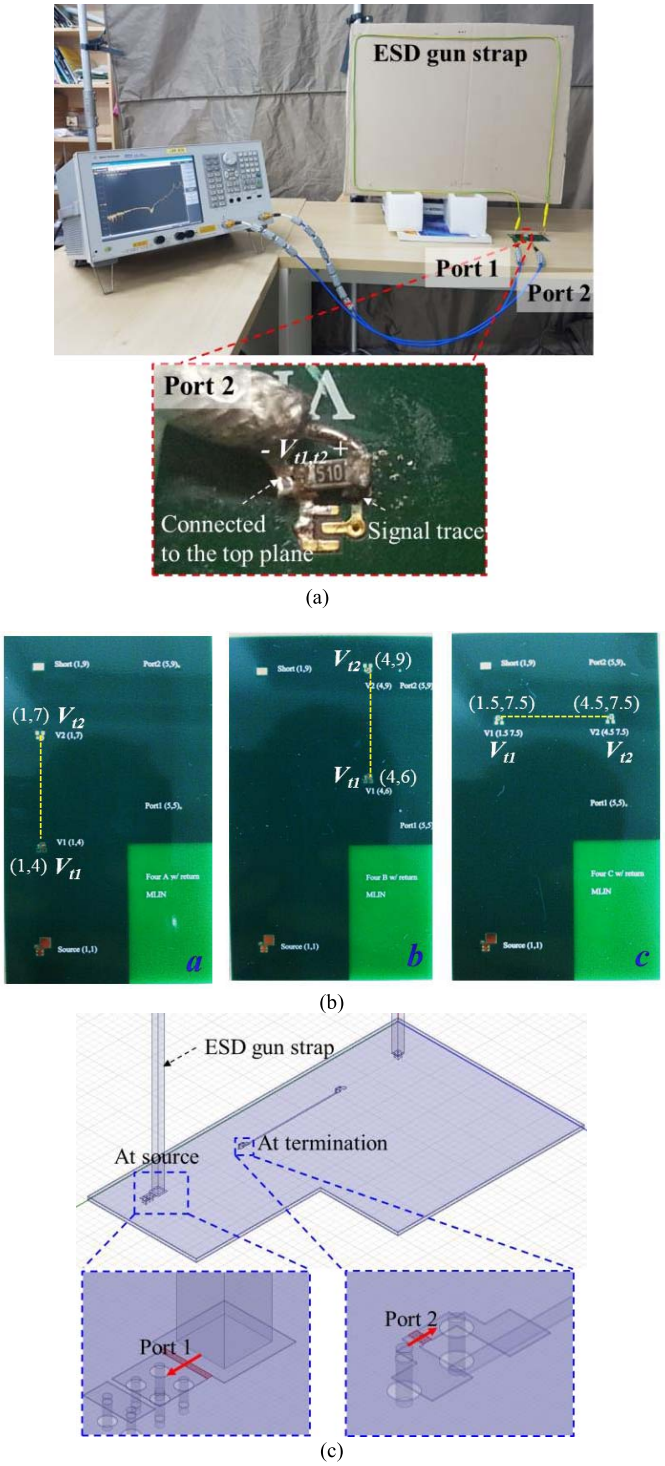

Fig. 9. (a) Measurement setup. (b) PCB design with three victim positions. (c) HFSS simulation setup.

the transfer impedances show the inductive behavior at the low frequency range below 30 MHz. The overall shapes and the relative trends agree well except for the resonance peak under 100 MHz. The discrepancy in the resonance is attributed to the inaccurate modeling of the strap geometry.

The computational time of the proposed method and HFSS simulation are compared in Table II. Both the proposed calculations and the HFSS simulations were solved in the

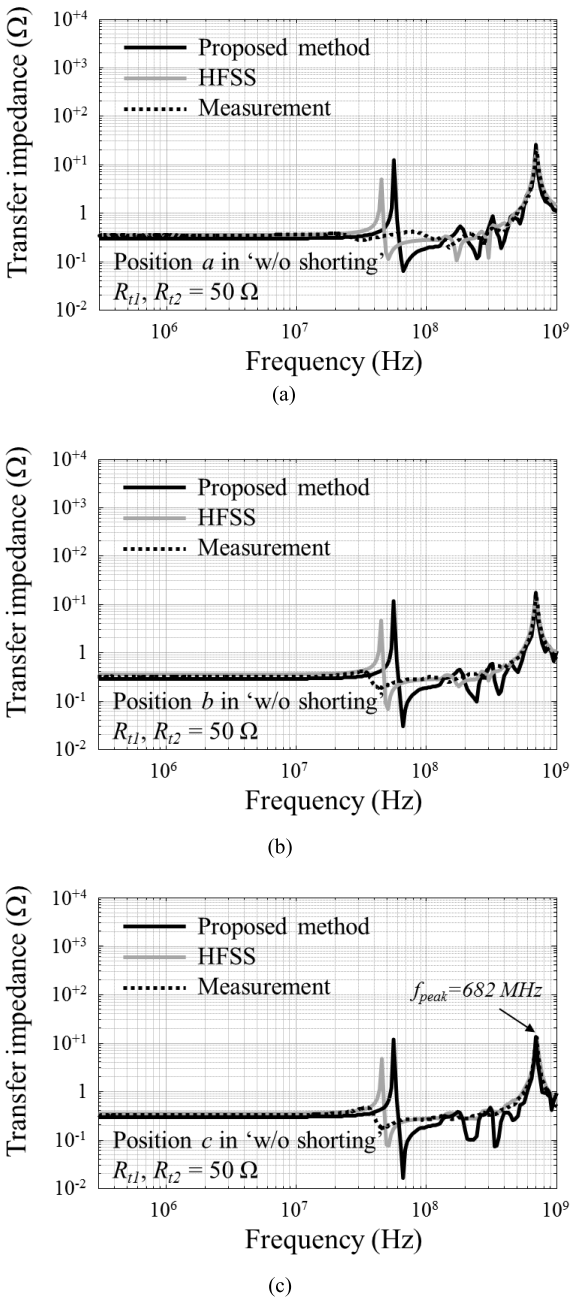

Fig. 10. Transfer impedances from the proposed method, HFSS, and measurement in the "w/o shorting" case. (a) Position *a*. (b) Position *b*. (c) Position *c*.

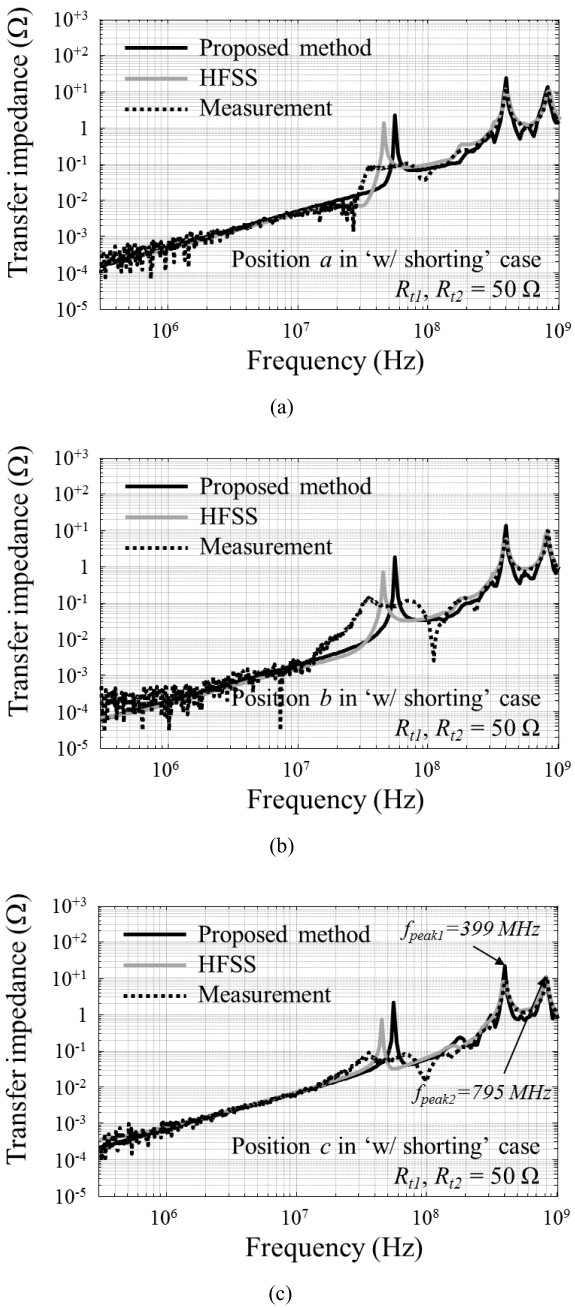

Fig. 11. Transfer impedance from the proposed method, HFSS, and measurement in the "w/ shorting" case. (a) Position *a*. (b) Position *b*. (c) Position *c*.

frequency domain with 201 points from 300 kHz to 1 GHz. A computer with 64-GB RAM and dual 2.4-GHz quad-core CPU was used in all the calculations.

Most of the calculation time in the proposed method is consumed to analyze the aggressor geometry. The aggressor structure is solved just once for multiple victim positions, which can greatly reduce the total computational time for various victim cases. For example, the proposed method takes 50 h 57 min 2 s to simulate the three victim cases in the "w/ shorting" case, whereas the HFSS simulation takes 189 h 45 min 1 s in total. When more victim cases are tested on an identical aggressor structure, the computational efficiency of the proposed method should be further improved. Also, the computational time for the aggressor PEEC model can be reduced if using sophisticated calculation techniques such as the adaptive meshing. The computational time for the total geometry using the full-wave PEEC is similar as that for only the aggressor geometry, since the model complexity is predominantly determined by the size of the aggressor structure. For example, the full-wave PEEC calculation takes 50 h 49 min 39 s, 50 h 46 min 31 s, and 50 h 49 min 17 s for positions *a*, *b*, and *c* in the "w/ shorting" case, respectively.

V. Calculation and Validation of the System-Level ESD Coupled Waveform in Time Domain

The actual ESD noise couplings are also calculated in frequency domain and converted to time domain using the

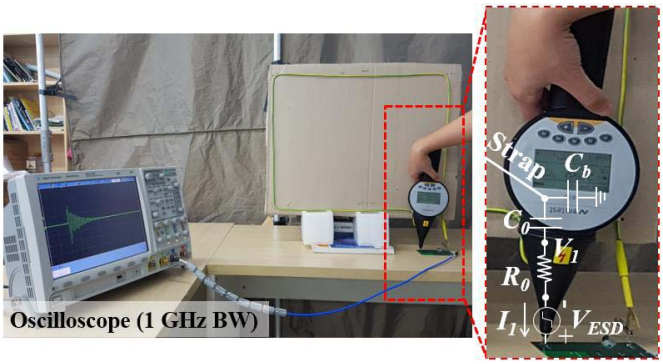

Fig. 12. Transient ESD test for the equivalent circuit of ESD generator.

inverse Fourier transform instead of the direct calculation in the time domain, since instability may occur at a very high frequency above our interests in the time domain retarded-PEEC analysis [27].

The contact discharging mode ESD generator was modeled as the series R–C circuits with 330 Ω and 150 pF in addition to a self-parasitic capacitance of the ESD gun body [28]. The self-capacitance of the ESD gun body is important to reproduce the high current peak with a fast rise time. The value of self-capacitance C_b is extracted as 9.6 pF from the 3-D *RLC* extractor, Ansys Q3D [29].

In the ESD measurement, there can be a direct electric field coupling from the ESD gun body to the signal pin of the rigid cable. Therefore, the signal pin of the rigid cable could be shielded using a copper tape to avoid direct coupling [29]. However, it has been confirmed that the direct coupling to the signal pin is insignificant here and no shielding structure was employed.

As explained in [9], the R–C discharging condition in the ESD gun can be effectively incorporated into the PEEC MNA equation in the frequency domain. The simple R–C model of the ESD generator with a voltage step pulse is combined with the PEEC aggressor model instead of the current source, as depicted in Fig. 12. V_1 is the voltage at the node between the capacitor and resistor, and I_1 is the ESD input current. In [9], assuming the ESD capacitor C_0 is initially charged to $V_1(0)$, the $C_0V_1(0)$ appears mathematically as the ESD source terms in the aggressor MNA equation. However, the rise time of the ESD injection current is not limited in the model, whereas the rise time is controlled by a rise time filter in an actual ESD gun [4]. After the parasitic capacitance of the gun body is properly included in the model, the calculated initial peaks in the ESD coupled voltages are too large without including the rise time of the ESD current. Therefore, instead of the initial voltage condition in the PEEC model, the ESD event is excited by a voltage step pulse with a proper rise time here [2]–[8].

A voltage step pulse with a rise time can be expressed in the time and frequency domains, respectively, as

$$V_{\mathrm{ESD}}(t) = \frac{V_{\mathrm{zap}}}{t_r} t u(t_r - t)u(t) + V_{\mathrm{zap}} u(t - t_r) \tag{18}$$

$$V_{\mathrm{ESD}}(s) = \frac{V_{\mathrm{zap}}(1 - e^{-t_r s})}{t_r s^2} \tag{19}$$

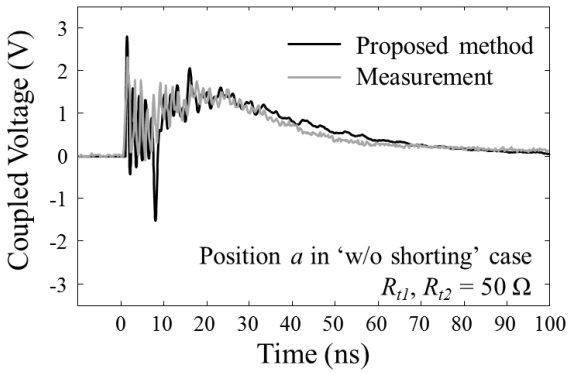

(a)

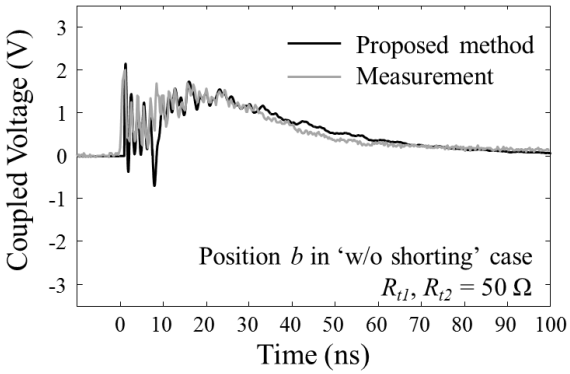

(b)

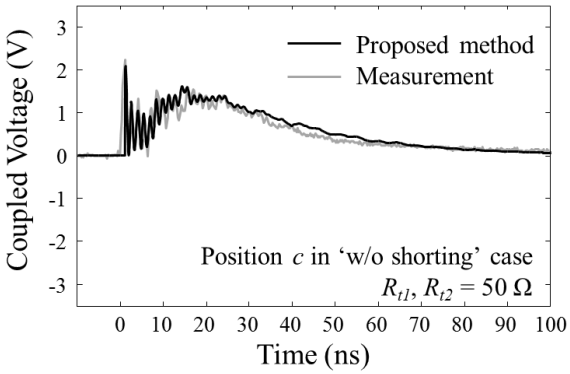

(c)

Fig. 13. ESD coupling waveform at termination V_{t1} in the "w/o shorting" case. (a) Position a. (b) Position b. (c) Position c.

where V_{zap} represents the ESD zap voltage, and t_r represents the rise time of the step function.

The aggressor MNA equation (9) is then modified to include the circuit components and the voltage step pulse of the ESD generator as (20), shown at the bottom of the next page.

As a result, the frequency spectra of the transient ESD charges and currents on the aggressor geometry can be obtained from the solution vector of (20). The ESD MNA matrix for the aggressor is solved from DC to 1 GHz with the linear frequency step of 5 MHz for analyzing the ESD event up to 200 ns. The calculated spectra of the ESD charges and currents in the aggressor are used as the coupling sources in the proposed victim calculation. The transient waveforms of ESD

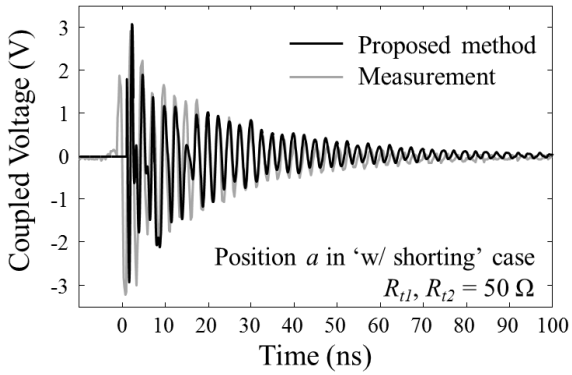

(a)

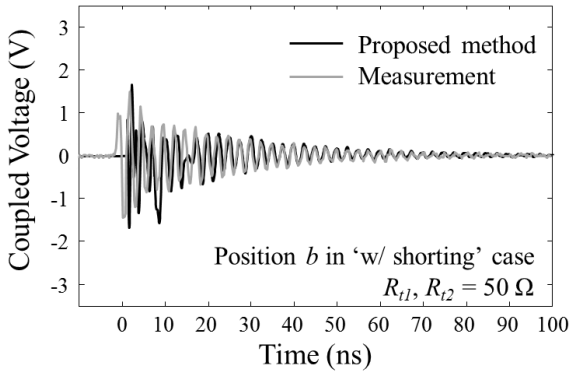

(b)

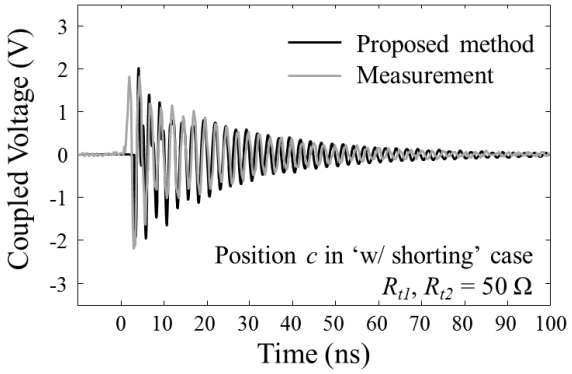

(c)

Fig. 14. ESD coupling waveform at termination V_{t1} in the "w/ shorting" case. (a) Position a. (b) Position b. (c) Position c.

coupling are obtained from the frequency spectra using inverse Fourier transform. Figs. 13 and 14 show the calculated and measured voltage waveforms at the termination V_{t1} induced by a 2-kV ESD event. The oscilloscope with 1-GHz bandwidth is used in all the measurements.

TABLE III
COMPARISON OF THE PEAK VOLTAGE AND THE RINGING FREQUENCY

		Proposed Method		Measurement		Error (%)	
		V_{peak} (V)	$f_{reso.}$ (MHz)	V_{peak} (V)	$f_{reso.}$ (MHz)	V_{peak}	$f_{reso.}$
w/o shorting	a	2.815	690.6	2.313	695	17.8	0.64
	b	2.155	690.6	2.000	690	7.2	0.09
	c	2.085	690.6	2.250	695	7.9	0.64
w/ shorting	a	3.076	399.8	2.906	395	5.5	1.20
	b	1.664	399.8	1.500	395	9.9	1.20
	c	2.017	399.8	1.813	395	10.1	1.20

The peak voltages, overall shapes, and duration of the waveform are quite similar between the calculations and measurements. The positive peaks and the dominant ringing frequencies are compared between the calculations and measurements in Table III. The ringing frequency and waveform shapes can be analyzed from the frequency domain results in Section IV. In the victim position c of the "w/o shorting" case, the transfer impedance has the highest peak at 682 MHz, as shown in Fig. 10(c). It is matched well with the fast ringing frequency of 695 MHz in the measured waveform of Fig. 13(c). The slow bump shape of the coupled voltages in the "w/o shorting" cases, which resembles the ESD input current pulse, is due to the constant transfer impedance below 30 MHz. In the victim position c of the "w/ shorting" case, the 400 MHz ringing frequency observed in the measured waveform in Fig. 14(c) is originated from the transfer impedance peak at 399 MHz in Fig. 11(c).

VI. CONCLUSION

ESD is one of the most critical noisy events that can cause malfunctions of ICs in electronic systems. A fast and accurate calculation method for system-level ESD noise coupling analysis was rigorously derived based on the PEEC model decomposition. The mathematical and physical process for developing the victim TLM affected by the large ESD structure was articulated and validated step-by-step. The computational time was compared with the commercial full-wave solver. The proposed method is very efficient without loss of accuracy, especially when various victim cases are analyzed in the same aggressor structure. The proposed method can be applied to find the best position or route of the signal trace in numerous design choices.

For calculation of the ESD coupling waveforms, the ESD generator circuit model was incorporated in the aggressor MNA equation, and the ESD transient waveforms on the victim signal trace were obtained from the frequency spectra of the charges and currents on the aggressor geometry. The overall shapes and the trends in various victim positions are

$$\begin{bmatrix} sC_0 & -sC_0\overline{N_{sg}}\,\overline{\overline{P_{a-a,r}}} & 1 & \bar{0} \\ -sC_0\overline{N_{sg}}^T & s\overline{\overline{E}} + s(C_0+C_b)\overline{N_{sg}}^T\,\overline{N_{sg}}\,\overline{\overline{P_{a-a,r}}} & -\overline{N_s}^T & -\overline{\overline{N_{m,a}}}^T \\ -1 & \overline{N_s}\,\overline{\overline{P_{a-a,r}}} & R_0 & \bar{0} \\ \bar{0}^T & \overline{\overline{N_{m,a}}}\,\overline{\overline{P_{a-a,r}}} & \bar{0}^T & \overline{\overline{Z_{a-a,r}}} \end{bmatrix} \begin{bmatrix} V_1 \\ \overline{Q_{a1}}^T \\ I_1 \\ \overline{I_{a1}}^T \end{bmatrix} = \begin{bmatrix} sC_0V_{\mathrm{ESD}}(s) \\ -sC_0V_{\mathrm{ESD}}(s)\overline{N_{sg}}^T \\ 0 \\ \bar{0}^T \end{bmatrix} \tag{20}$$

quite similar between the calculations and measurements. The ringing frequency and shapes of the ESD transient waveforms can be analyzed from the transfer impedances in the frequency domain. The proposed calculation method has high efficiency and possibility to be used for various kinds of system noise coupling problems.

REFERENCES

[1] H. W. Ott, *Electromagnetic Compatibility Engineering*. Hoboken, NJ, USA: Wiley, 2009.

[2] D. Liu *et al.*, "Full-wave simulation of an electrostatic discharge generator discharging in air-discharge mode into a product," *IEEE Trans. Electromagn. Compat.*, vol. 53, no. 1, pp. 28–37, Feb. 2011.

[3] J. Xiao *et al.*, "Model of secondary ESD for a portable electronic product," *IEEE Trans. Electromagn. Compat.*, vol. 54, no. 3, pp. 546–555, Jun. 2012.

[4] K. Wang, D. Pommerenke, R. Chundru, T. V. Doren, J. L. Drewniak, and A. Shashindranath, "Numerical modeling of electrostatic discharge generators," *IEEE Trans. Electromagn. Compat.*, vol. 45, no. 2, pp. 258–271, May 2003.

[5] S. Caniggia and F. Maradei, "Circuit and numerical modeling of electrostatic discharge generators," *IEEE Trans. Ind. Appl.*, vol. 42, no. 6, pp. 1350–1357, Nov./Dec. 2006.

[6] F. Centola, D. Pommerenke, W. Kai, T. Van Doren, and S. Caniggia, "ESD excitation model for susceptibility study," in *Proc. IEEE Int. Symp. Electromagn. Compat.*, vol. 1. Aug. 2003, pp. 58–63.

[7] M. Angeli and E. Cardelli, "Numerical modeling of electromagnetic fields generated by electrostatic discharges," *IEEE Trans. Magn.*, vol. 33, no. 2, pp. 2199–2202, Mar. 1997.

[8] S. Caniggia and F. Maradei, "Numerical prediction and measurement of ESD radiated fields by free-space field sensors," *IEEE Trans. Electromagn. Compat.*, vol. 49, no. 3, pp. 494–503, Aug. 2007.

[9] J. Park, J. Lee, B. Seol, and J. Kim, "Efficient calculation of inductive and capacitive coupling due to electrostatic discharge (ESD) using PEEC method," *IEEE Trans. Electromagn. Compat.*, vol. 57, no. 4, pp. 743–753, Aug. 2015.

[10] J. Park, J. Lee, S. Kim, B. Seol, and J. Kim, "Fast calculation of system-level ESD noise coupling to a microstrip line using PEEC method," in *Proc. IEEE Int. Symp. Elect. Design Adv. Packag. Syst.*, Seoul, South Korea, Dec. 2015, pp. 132–135.

[11] J. Park *et al.*, "Modeling and measurement of simultaneous switching noise coupling through signal via transition," *IEEE Trans. Adv. Packag.*, vol. 29, no. 3, pp. 548–559, Aug. 2006.

[12] J. Kim, M. D. Rotaru, S. Baek, J. Park, M. K. Iyer, and J. Kim, "Analysis of noise coupling from a power distribution network to signal traces in high-speed multilayer printed circuit boards," *IEEE Trans. Electromagn. Compat.*, vol. 48, no. 2, pp. 319–330, May 2006.

[13] Z. Z. Oo *et al.*, "A semi-analytical approach for system-level electrical modeling of electronic packages with large number of vias," *IEEE Trans. Adv. Packag.*, vol. 31, no. 2, pp. 267–274, May 2008.

[14] G. Feng and J. Fan, "An extended cavity method to analyze slot coupling between printed circuit board cavities," *IEEE Trans. Electromagn. Compat.*, vol. 53, no. 1, pp. 140–149, Feb. 2011.

[15] X.-C. Wei and E.-P. Li, "Integral-equation equivalent-circuit method for modeling of noise coupling in multilayered power distribution networks," *IEEE Trans. Microw. Theory Techn.*, vol. 58, no. 3, pp. 559–565, Mar. 2010.

[16] L. K. Yeung and K.-L. Wu, "Generalized partial element equivalent circuit (PEEC) modeling with radiation effect," *IEEE Trans. Microw. Theory Techn.*, vol. 59, no. 10, pp. 2377–2384, Oct. 2011.

[17] F. Zhou, A. E. Ruehli, and J. Fan, "Efficient mid-frequency plane inductance computation," in *Proc. IEEE Int. Symp. Electromagn. Compat.*, Fort Lauderdale, FL, USA, Aug. 2010, pp. 831–836.

[18] A. E. Ruehli and P. A. Brennan, "Efficient capacitance calculations for three-dimensional multiconductor systems," *IEEE Trans. Microw. Theory Techn.*, vol. 21, no. 2, pp. 76–82, Feb. 1973.

[19] G. Antonini, S. Cristina, and A. Orlandi, "PEEC modeling of lightning protection systems and coupling to coaxial cables," *IEEE Trans. Electromagn. Compat.*, vol. 40, no. 4, pp. 481–491, Nov. 1998.

[20] A. E. Ruehli and H. Heeb, "Circuit models for three-dimensional geometries including dielectrics," *IEEE Trans. Microw. Theory Techn.*, vol. 40, no. 7, pp. 1507–1516, Jul. 1992.

[21] F. W. Grover, *Inductance Calculations: Working Formulas and Tables*. New York, NY, USA: Dover, 1946.

[22] D. M. Pozar, *Microwave Engineering*, 4th ed. New York, NY, USA: Wiley, 2012.

[23] *Design Guide for Packaging of High Speed Electronic Circuits*, IPC, Northbrook, IL, USA, Nov. 2003, p. 32.

[24] Y.-J. Zhang and J. Fan, "An intrinsic circuit model for multiple vias in an irregular plate pair through rigorous electromagnetic analysis," *IEEE Trans. Microw. Theory Techn.*, vol. 58, no. 8, pp. 2251–2265, Aug. 2010.

[25] J. Kim, J. Fan, A. E. Ruehli, J. Kim, and J. L. Drewniak, "Inductance calculations for plane-pair area fills with vias in a power distribution network using a cavity model and partial inductances," *IEEE Trans. Microw. Theory Techn.*, vol. 59, no. 8, pp. 1909–1924, Aug. 2011.

[26] A. E. Ruehli, C. Paul, and J. Garrett, "Inductance calculations using partial inductances and macromodels," in *Proc. IEEE Int. Symp. Electromagn. Compat.*, Aug. 1995, pp. 23–28.

[27] A. E. Ruehli, U. Miekkala, and H. Heeb, "Stability of discretized partial element equivalent EFIE circuit models," *IEEE Trans. Antennas Propag.*, vol. 43, no. 6, pp. 553–559, Jun. 1995.

[28] *Electromagnetic Compatibility (EMC)—Part 4-2: Testing and Measurement Techniques—Electrostatic Discharge Immunity Test*, Doc. IEC 61000-4-2:2008, Dec. 2008.

[29] M. Park *et al.*, "Measurement and modeling of system-level ESD noise voltages in real mobile products," in *Proc. Asia-Pacific Symp. Electromagn. Compat.*, Shenzhen, China, May 2016, pp. 632–634.

Junsik Park received the B.S. degree in electrical engineering from the Ulsan National Institute of Science and Technology, Ulsan, South Korea, in 2014, where he is currently pursuing the Ph.D. degree.

His current research interests include the partial element equivalent circuit and electrostatic discharge.

Jongsung Lee received the B.S. and M.S. degrees in electrical engineering from the University of California at Irvine, Irvine, CA, USA, in 2002 and 2004, respectively.

Since 2004, he has been with Samsung Electronics, Suwon, South Korea. His current research interests include electrostatic discharge and electromagnetic compatibility in both system level and factory issues.

Byongsu Seol received the B.S. and M.S. degrees from Chungbuk National University, Cheongju, South Korea, in 1992 and 1995, respectively.

From 1993 to 1994, he was with the University of Arizona, Tucson, AZ, USA, where he was involved in the development of transmission line parameter extraction programs. In 1994, he joined the IC Packaging Technology Group, LG Semicon, Cheongju, which later became a part of SK Hynix. In 2000, he joined Tessera Technologies, San Jose, CA, USA, as a Signal Integrity Engineer. Since 2002, he has been with Samsung Electronics, Suwon, South Korea. His current research interests include high-speed system designs, electromagnetic interference/electromagnetic compatibility, electrostatic discharge analysis methods, and sensor and sensing technologies for electronic products and smart factory applications.

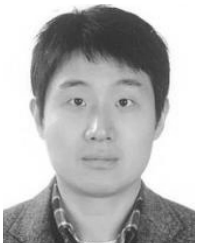

Jingook Kim (M'09–SM'15) received the B.S., M.S., and Ph.D. degrees in electrical engineering from the Korea Advanced Institute of Science and Technology, Daejeon, South Korea, in 2000, 2002, and 2006, respectively.

From 2006 to 2008, he was a Senior Engineer with the DRAM Design Team, Memory Division, Samsung Electronics, Hwasung, South Korea. From 2009 to 2011, he was a Post-Doctoral Fellow with the Electromagnetic Compatibility (EMC) Laboratory, Missouri University of Science and Technology, Rolla, MO, USA. In 2011, he joined the Ulsan National Institute of Science and Technology, Ulsan, South Korea, where he is currently an Associate Professor. His current research interests include high-speed I/O circuits design, 3-D IC, EMC, electrostatic discharge, and RF interference.